Thermo X

Science Exploration

Open Access Research Article

# Transient thermal response and regulation of transparent silica aerogels under fluctuating solar irradiance

Shiteng Li[1,2,3,4], Ningxin Yang[1,2], Fujie Li[1,2], Shang Liu[1,2], Chun Li[1,2], Shuai Deng[3,4,*], Meng Lin[1,2,*]

[1]Department of Mechanical and Energy Engineering, Southern University of Science and Technology, Shenzhen 518055, Guangdong, China.
[2]SUSTech Energy Institute for Carbon Neutrality, Southern University of Science and Technology, Shenzhen 518055, Guangdong, China.
[3]State Key Laboratory of Engines, Tianjin University, Tianjin 300350, China.
[4]National Industry-Education Platform for Energy Storage (Tianjin University), Tianjin 300350, China.

***Correspondence to:** Shuai Deng, State Key Laboratory of Engines, Tianjin University, Tianjin 300350, China. National Industry-Education Platform for Energy Storage (Tianjin University), Tianjin 300350, China. E-mail: sdeng@tju.edu.cn
Meng Lin, Department of Mechanical and Energy Engineering, Southern University of Science and Technology, Shenzhen 518055, Guangdong, China; SUSTech Energy Institute for Carbon Neutrality, Southern University of Science and Technology, Shenzhen 518055, Guangdong, China. E-mail: linm@sustech.edu.cn

**Received:** August 13, 2026 **Accepted:** October 16, 2026 **Published:** October 16, 2026

**Cite this article:** Li S, Yang N, Li F, Liu S, Li C, Deng S, et al. Transient thermal response and regulation of transparent silica aerogels under fluctuating solar irradiance. Thermo-X. 2027;3:202636. https://doi.org/10.70401/tx.2026.0039

## Abstract

Transparent silica aerogels can reduce heat loss from solar receivers while maintaining high solar transmission, but their performance under fluctuating irradiation is governed by the coupled effects of solid conduction, non-gray thermal radiation, and time-dependent fluid heat extraction. Here, we develop and experimentally validate a transient 5-band model for an aerogel-covered solar receiver for fluid heating. The model resolves wavelength-dependent radiative transport within the aerogel and couples it with heat conduction and forced convection. We show that conduction and radiation cannot be reconstructed from isolated calculations because both adjust to a shared temperature field. The coupled heat flux at the aerogel-absorber interface is 23-31% lower than the directly superposed value, while appearing accurate at the external aerogel surface because the internal coupling effects compensate spatially. Flow regulation introduces a further trade-off between outlet temperature rise and response speed. Simulations driven by measured global horizontal irradiance in Shenzhen show that the flow adjustment interval mainly controls short-term temperature stability, whereas the irradiation regime and periods of flow interruption dominate the integrated thermal performance. These results establish a transport-based framework for understanding and regulating transparent aerogel covered solar receivers under variable solar input.

**Keywords:** Transparent silica aerogel, transient heat transfer, participating medium radiation, conduction-radiation coupling, solar fluid heating, flow regulation

## 1. Introduction

Solar thermal receivers operate under an intrinsically variable energy input[1,2]. Cloud passages, diurnal variation, and intermittent shading alter the absorbed solar power over timescales ranging from seconds to hours, while the receiver, insulation, and heat transfer fluid respond according to their own thermal inertia[3-5]. Transparent silica aerogels are attractive covers for such receivers because they combine high solar transmittance with low solid thermal conductivity and strong attenuation of long-wave thermal radiation[6-9]. These properties have enabled unconcentrated solar heating above 200 °C and have improved the thermal performance of solar evaporation systems[3,10-12]. Recent work has further shown that the optical response of transparent aerogels can be tuned through their multiscale porous structure[13]. Transparent aerogels have also been investigated in several solar thermal receiver configurations using coupled optical-thermal simulations[14-16]. These studies demonstrated the potential of aerogel integration for reducing thermal losses and improving receiver performance and highlighted the importance of accounting for the wavelength dependent optical and radiative behavior of aerogels in receiver modeling[14-16]. However, most existing investigations focused on steady-state performance, receiver efficiency, or structural optimization[14-16]. The transient evolution of coupled conduction and non-gray radiation within the aerogel under varying solar input remains insufficiently quantified. Most analyses, however, focus on steady operation or report an effective overall heat-loss coefficient. Such treatments do not directly resolve how heat is redistributed inside the aerogel when the solar input changes with time.

© The Author(s) 2026. This is an Open Access article licensed under a Creative Commons Attribution 4.0 International License (https://creativecommons.org/licenses/by/4.0/), which permits unrestricted use, sharing, adaptation, distribution and reproduction in any medium or format, for any purpose, even commercially, as long as you give appropriate credit to the original author(s) and the source, provide a link to the Creative Commons license, and indicate if changes were made.

The internal heat transfer is particularly difficult to simplify because transparent silica aerogels are non-gray participating media in the thermal infrared range. Their absorption coefficient varies strongly with wavelength, hence radiation emitted by the hot absorber can penetrate different distances before being absorbed within the aerogel[17,18]. This volumetric energy deposition modifies the temperature field that drives solid conduction. In turn, conduction changes the local temperature and therefore the emission and absorption of thermal radiation. Conduction and radiation are linked through a shared temperature field rather than acting as two independent parallel paths. Studies of coupled participating media have shown that adding separately calculated conductive and radiative heat fluxes can produce substantial errors because the isolated calculations correspond to different thermal states[19,20]. For an aerogel covered solar receiver, it remains unclear how this non-additivity evolves during a change in irradiation, how strongly it depends on operating temperature, and whether an apparently accurate heat flux at the exposed surface can conceal a much larger error near the absorber.

Useful heat extraction adds a second dynamic constraint. Increasing the fluid flow rate raises the heat-capacity rate and shortens the residence time, which reduces the outlet temperature rise but can accelerate the response to a change in solar input. Dynamic solar collector studies have long recognized that the measured outlet temperature reflects both the instantaneous input and the stored thermal energy of the collector[21,22]. A characteristic response time is therefore needed to distinguish solar fluctuations that are filtered by receiver inertia from sustained changes that require active adjustment[23]. A steady operating map can relate irradiation and flow rate to a target outlet temperature, but applying this map under real weather requires choosing an update interval[24]. Updating much faster than the receiver can respond may repeatedly change the setpoint before the outlet reacts, while slow updating delays adaptation to meaningful changes. The relationship among flow rate, response time, update interval, and integrated thermal efficiency has not been established for transparent aerogel covered receivers.

This study combines experiments and transient multiphysics modeling to resolve how coupled heat transfer and thermal inertia govern the performance of transparent silica aerogel-covered solar receivers under variable irradiation. The model is first validated against stagnation measurements and then used to quantify the non-additive interaction between conduction and non-gray thermal radiation during an irradiation step, with particular attention to the distinct responses at the aerogel-absorber interface and the exposed aerogel surface. The same framework is extended to fluid heating to reveal how flow rate simultaneously affects outlet temperature lift and thermal response time. Using measured global horizontal irradiance (*GHI*) profiles, we further assess how these intrinsic response times interact with flow-adjustment intervals of 60–300 s under realistic solar fluctuations. The resulting framework connects internal transport mechanisms with the dynamic operating constraints of aerogel covered solar thermal systems.

## 2. Methods

### 2.1 Experimental characterization and stagnation test

The optical and thermal properties required for the numerical model were determined experimentally. The total spectral transmittance of the transparent silica aerogel and the total spectral reflectance of the nanocarbon coated copper absorber were measured over 250–2,500 nm using a UV-visible-near infrared spectrophotometer equipped with an integrating sphere (LAMBDA 750S, PerkinElmer). Because the absorber was opaque over this wavelength range, its spectral absorptance was obtained from the measured reflectance. The solar weighted aerogel transmittance and absorber absorptance were calculated using the AM 1.5G solar spectrum. The effective thermal conductivity of the silica aerogel was measured using a custom steady state heat flow meter with hot and cold plate temperatures of 33 and 13 °C, respectively.

For transient model validation, a 30 mm × 30 mm × 0.3 mm solar absorber was covered by a 30 mm × 30 mm × 12.6 mm transparent silica aerogel. The bottom and lateral surfaces were insulated, and the incident irradiance at the absorber plane was calibrated to 1,000 W $m^{-2}$ using a photoradiometer (PL-MW2000, Beijing Perfectlight Technology Co., Ltd., China). K-type thermocouples were positioned at the center of the absorber surface beneath the aerogel and at the center of the upper aerogel surface. The temperatures were recorded using a TC-08 data acquisition module for 7,200 s from the onset of solar irradiation. Detailed sample preparation, characterization procedures, and the experimental setup are provided in Supporting Note S1.

### 2.2 Model framework and validation

The physical configuration and the principal energy-transfer processes considered in the model are summarized in Figure 1. A two-dimensional (2D) transient finite element model was formulated for a solar fluid heater consisting of a transparent silica aerogel cover with a porosity of 91%, an opaque solar absorber, surrounding insulation, and, when active, an underlying liquid channel. Two operating configurations were derived from the same physical framework. The stagnation configuration contained the aerogel, absorber, and insulation and was used for experimental validation, heat loss analysis, and conduction-radiation diagnostics. The fluid flow configuration added the liquid channel and was used to evaluate outlet temperature response, steady operating maps, and dynamic flow regulation. The experimental setup used for stagnation validation is shown in Figure S1, while detailed sample preparation and characterization procedures are provided in Supporting Note S1.

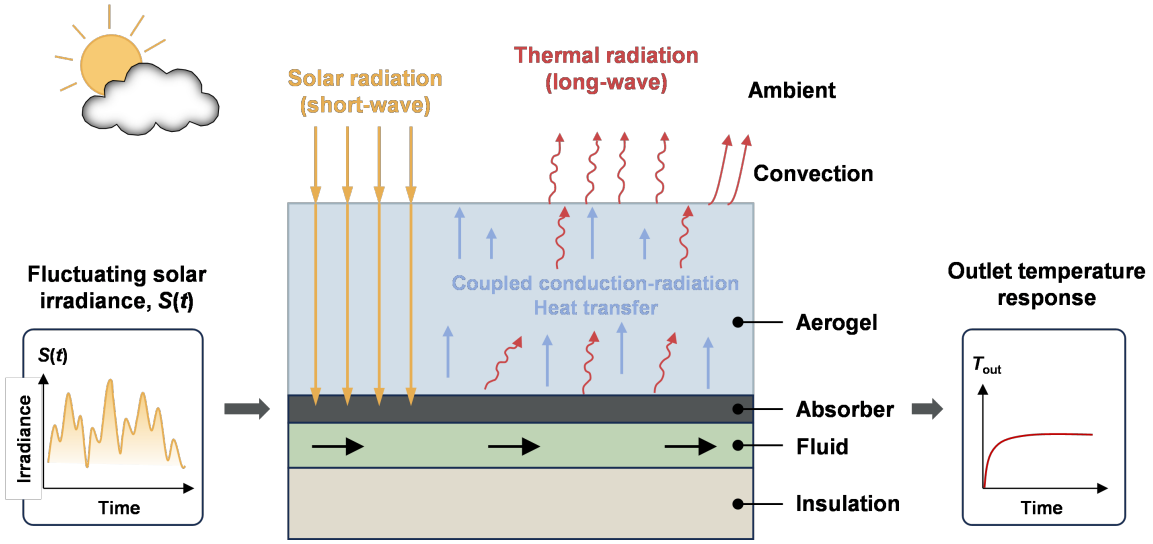


**Figure 1.** Physical framework and model configurations for an aerogel covered solar fluid heater under fluctuating irradiance.

The model accounted for transient heat storage and conduction in the aerogel, absorber, and insulation, non-gray thermal radiation transport within the aerogel, conjugate heat transfer between the absorber and working fluid (silicone oil), incompressible laminar flow, and convective and radiative heat exchange with the surroundings. Short-wave solar input and long-wave thermal radiation were treated separately because they occupy different wavelength ranges and govern different energy transfer processes. The solar flux deposited at the absorber was calculated as

$$q_{\text{solar}}''(t) = S(t)\tau_{\text{solar}}\,\alpha_{\text{abs}} \tag{1}$$

where $S(t)$ is the incident irradiance, $\tau_{\text{solar}}$ is the measured solar weighted total transmittance of the aerogel, and $\alpha_{\text{abs}}$ is the measured solar absorptance of the absorber. Long-wave radiation emitted by the heated absorber was resolved inside the aerogel using a non-gray participating medium formulation. The continuous infrared absorption spectrum was reduced to 5 spectral bands that retain the principal transparent windows and strong silica absorption regions. Long-wave scattering was neglected. The calculation of the infrared radiative properties, the 5-band spectral discretization, and the corresponding independence analysis are detailed in Supporting Note S3, Table S3, and Figure S4.

The aerogel was represented as a homogeneous and isotropic effective continuum with a single temperature field. The effective properties were taken as spatially uniform, the absorber was treated as opaque, and the working fluid was modeled as single phase, incompressible, and laminar. Gravity and buoyancy were neglected. Solar irradiance was assumed to be spatially uniform over the illuminated absorber. Perfect thermal contact was imposed between adjacent domains, and out-of-plane gradients were neglected in the 2D representation. Because the finite lateral dimensions of the validation specimen introduce additional edge heat losses, the subsequent 2D stagnation calculations employed a calibrated effective thermal conductivity for the insulation ($k_{\text{eff}}$) to account for out-of-plane heat spreading and finite edge losses that are not explicitly resolved in the 2D formulation. The full 3D assessment and calibration procedure are provided in Section S4.5 and Figures S8–S11.

The governing heat transfer, radiative transfer, and fluid flow equations were solved using COMSOL Multiphysics 6.1. The model was first validated under constant irradiance by comparing the calculated absorber and upper aerogel surface temperatures with measurements under stagnation. Agreement in both the transient heating trajectory and steady temperature was established before the model was applied to the transport coupling and flow regulation analyses. Detailed governing equations, computational domains, initial and boundary conditions, and thermophysical properties are provided in Supporting Note S2 and Table S2. The spectral treatment is described in Supporting Note S3, while the numerical implementation and independence analyses are provided in Supporting Note S4 and Figures S5–S7.

## 2.3 Transport coupling and dynamic response metrics

Three diagnostic heat transfer cases were derived from the stagnation configuration. The fully coupled case retained both solid conduction and participating medium thermal radiation within the aerogel. In the conduction only case, participating medium radiation and its coupling to the energy equation were deactivated, while external radiative heat loss to the surroundings was retained. In the radiation only case, participating medium radiation was retained and the aerogel thermal conductivity was set to 0. The isolated cases are diagnostic limits rather than physically realizable receivers.

For each evaluation location, direct superposition of the isolated heat fluxes was defined as

$$q_{\text{sup},j}'' = q_{\text{cond only},j}'' + q_{\text{rad only},j} \tag{2}$$

The coupling factor was calculated as[20]

$$f_j = \frac{q_{\text{coupled},j}''}{q_{\text{sup},j}''} = \frac{q_{\text{cond, coupled},j}'' + q_{\text{rad, coupled},j}''}{q_{\text{cond only},j}'' + q_{\text{rad only},j}''} \tag{3}$$

A value of $f_j = 1$ indicates that direct addition of the isolated cases reproduces the fully coupled heat flux. Departure from unity quantifies non-additivity associated with the different temperature fields established in the isolated and coupled cases. The radiative fraction in the coupled case was defined as[20]

$$\xi_j = \frac{q_{\text{rad,coupled},j}''}{q_{\text{cond,coupled},j}'' + q_{\text{rad,coupled},j}''} \tag{4}$$

The metrics were evaluated at the aerogel-absorber interface and the upper aerogel boundary, as illustrated in Figure S13.

The transient outlet response was characterized from step changes in irradiance at fixed inlet velocities. The normalized outlet temperature response was

$$\theta_{\text{out}}(t) = \frac{T_{\text{out}}(t) - T_{\text{out},i}}{T_{\text{out},f} - T_{\text{out},i}} \tag{5}$$

where $T_{\text{out}}(t)$ is the instantaneous outlet temperature, and $T_{\text{out},i}$ and $T_{\text{out},f}$ are the initial and final steady outlet temperatures, respectively. The characteristic outlet response time was defined using the conventional 63.2% criterion[23]

$$\theta_{\text{out}}(t_0 + \tau_{\text{out}}) = 1 - e^{-1} \tag{6}$$

where $t_0$ is the time of the irradiance step, and the normalized temperature response reaches 0.632, corresponding to 63.2% of the total temperature change. This operational definition was applied directly to the calculated response and did not require the complete transient to follow an exact single exponential function. Heating and cooling response times were evaluated separately. The step response protocol, response time extraction procedure, and complete response metrics are provided in Supporting Note S6 and Tables S4,S5.

### 2.4 Flow regulation under fluctuating solar irradiance

A steady operating map was generated by calculating the outlet temperature over combinations of incident irradiance and inlet velocity.

$$T_{\text{out,ss}} = F(S, v_{\text{in}}) \tag{7}$$

where $F$ is the steady operating map, and $v_{\text{in}}$ is the inlet fluid velocity. For a prescribed outlet temperature target, the required inlet velocity was obtained by inverting the map.

$$v_{\text{set}} = F^{-1}(S, T_{\text{target}}) \tag{8}$$

where $T_{\text{target}}$ is the target outlet temperature, and the $T_{\text{target}} = 50$ °C. Measured *GHI* was sampled at adjustment intervals ($\Delta_{\text{adj}}$) of 60, 120, 180, 240, or 300 s. At each update, the corresponding velocity was selected from the operating map and held until the next update. Flow was stopped when *GHI* was below 262.5 W m$^{-2}$ because the target temperature could not be maintained within the investigated operating range. The minimum nonzero inlet velocity was $2 \times 10^{-4}$ m s$^{-1}$. Consecutive setpoints were connected by a 5 s continuously differentiable cubic ramp.

$$v_{\text{in}}(t) = v_i + (v_{i+1} - v_i)\left(3\phi^2 - 2\phi^3\right), \quad 0 \le \phi \le 1 \tag{9}$$

where $\phi = (t - t_i)/t_r$, $t_i$ is the update time, $t_r = 5$ s is the ramp duration, and $v_i$ and $v_{i+1}$ are two consecutive inlet velocity setpoints. The outlet temperature used for thermal power calculations was the mass-flow-weighted mean.

$$T_{\text{out,m}}(t) = \frac{\int_{A_{\text{out}}} \bar{\rho}_f (\mathbf{u}\cdot\mathbf{n}) T dA}{\int_{A_{\text{out}}} \bar{\rho}_f (\mathbf{u}\cdot\mathbf{n}) dA} \tag{10}$$

where $A_{\text{out}}$ is the outlet cross-sectional area, $\bar{\rho}_f$ is the fluid density, $\mathbf{u}$ is the velocity vector, $\mathbf{n}$ is the outward unit normal vector. The

instantaneous useful thermal power delivered to the liquid was:

$$\dot{Q}_u(t) = \dot{m}(t) c_{p,f} \left[ T_{\text{out,m}}(t) - T_{\text{in}} \right] \tag{11}$$

where $\dot{m}$ is the fluid mass flow rate, $c_{p,f}$ is the specific heat capacity of the fluid at constant pressure, $T_{\text{out,m}}$ is the mass-flow-weighted mean outlet temperature, and $T_{\text{in}}$ is the inlet fluid temperature. The integrated solar to thermal efficiency ($\eta_{\text{th}}$) over the evaluated period was:

$$\eta_{\text{th}} = \frac{\int_{t_s}^{t_e} \dot{Q}_u(t)\,\mathrm{d}t}{A_{\text{abs}} \int_{t_s}^{t_e} S(t)\,\mathrm{d}t} \tag{12}$$

where $\dot{Q}_u$ is the instantaneous useful thermal power delivered to the fluid, $A_{\text{abs}}$ is the absorber area, and $t_s$ and $t_e$ are the start and end times of the evaluation period, respectively. When flow was stopped, $\dot{m} = 0$ and no useful thermal output was counted. The denominator represents solar energy incident on the receiver, so optical loss through the aerogel and absorber, receiver heat loss, and ending stored energy are reflected in the reported efficiency. Hydraulic pumping power was not included, and $\eta_{\text{th}}$ is therefore a gross solar to useful heat efficiency.

## 3. Results and Discussion

### 3.1 Optical and radiative properties, stagnation validation, and heat loss pathways

The transparent silica aerogel prepared in this work had a porosity of 91%, a solar weighted total transmittance of 90%, and a thermal conductivity of 0.015 W $m^{-1}$ $K^{-1}$, while the absorber showed a solar absorptance of 98% (Figure 2a). This combination allows most incident solar energy to reach the underlying absorber while limiting conductive heat transfer through the cover. The measured solar transmittance and absorber absorptance were used to determine the solar heat deposited at the absorber, and the measured thermal conductivity was used directly in the heat transfer model. Details of the aerogel synthesis, absorber preparation, and optical and thermal characterization are provided in Sections S1.2–S1.4.

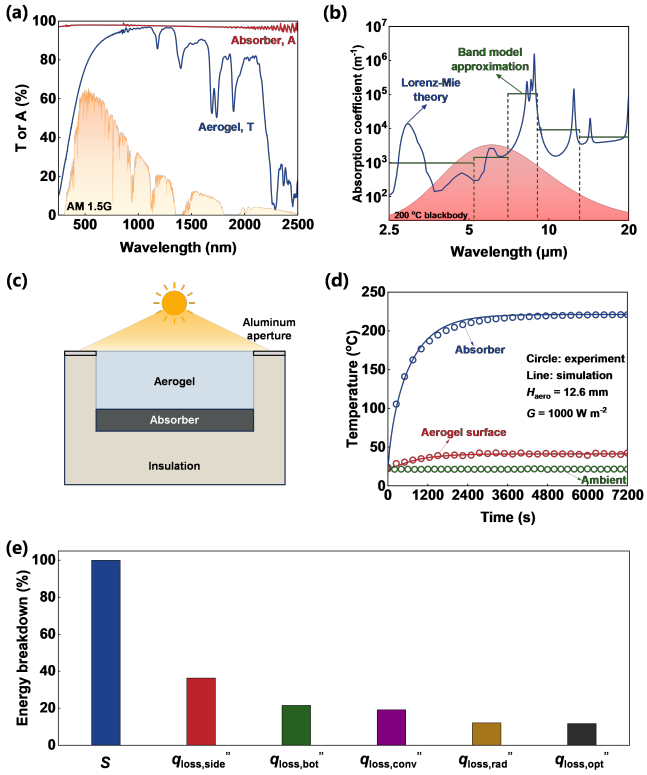


**Figure 2.** Optical properties and stagnation validation. (a) Absorber absorptance, aerogel transmittance, and AM 1.5G spectrum; (b) Infrared absorption coefficient and 5-band model; (c) Experimental configuration; (d) Measured and simulated temperatures at 1,000 W $m^{-2}$; (e) Steady state energy breakdown under stagnation.

The radiative properties of the aerogel are considerably more wavelength dependent in the thermal infrared range. As shown in Figure 2b, the absorption coefficient varies from $10^2$ $m^{-1}$ in relatively transparent spectral regions to nearly $10^6$ $m^{-1}$ within the

principal silica absorption bands between 2.5 and 20 μm. These variations overlap the emission spectrum of the absorber at the investigated temperatures and produce strongly wavelength-dependent radiative penetration through the aerogel. A gray approximation based on a single absorption coefficient would therefore be unable to represent both transparent windows and strongly absorbing regions.

The continuous infrared spectrum was represented using a 5-band model. The band boundaries and band-averaged absorption coefficients were selected to retain the major variations in the spectrum rather than individual narrow peaks. The suitability of this discretization was assessed against progressively refined spectral representations by comparing the absorber temperature, upper aerogel surface temperature, and computational cost. The corresponding band properties are listed in Table S3. Spectral band independence was further evaluated using 1, 3, 5, and 7 bands (Figure S4). Relative to the 7-band model, the 5-band representation produced maximum deviations of only 1.27 °C in absorber temperature and 0.20 °C in upper aerogel surface temperature. The 5-band model was therefore adopted for the subsequent transient calculations.

The transient model was validated under stagnation using the insulated configuration shown in Figure 2c. The experimental setup and corresponding computational domain are provided in Figures S1,S2, respectively. No fluid heat extraction was applied, so the incident energy was accommodated by transient heat storage and heat rejection through the aerogel covered surface and surrounding insulation. A 12.6-mm-thick aerogel was exposed to constant irradiance of 1,000 W $m^{-2}$, and the absorber and upper aerogel surface temperatures were monitored over 7,200 s.

As shown in Figure 2d, the measured absorber temperature increased from 22 °C to 218 °C, while the predicted temperature approached 220 °C. The model slightly overpredicted the absorber temperature during the intermediate heating period, with a maximum deviation of 7 °C, while the steady deviation was 2 °C. The measured external aerogel-surface temperature increased to 40–41 °C, compared with a predicted value of 42 °C. The steady state deviation in upper aerogel surface temperature remained within 2 °C over the heating period. The uncertainty associated with the experimental measurements is quantified in Section S1.6 and summarized in Table S1. The model therefore reproduced both the 200 °C absorber temperature rise and the much smaller 20 °C temperature rise at the exposed aerogel surface.

The simultaneous agreement at the 2 measurement locations constrains different parts of the receiver energy balance. The absorber temperature depends on transmitted solar input and total heat rejection from the heated surface, whereas the external aerogel-surface temperature is directly affected by heat transport across the aerogel and heat exchange with the environment. The 178 °C steady temperature difference between the absorber and aerogel surface is therefore captured without fitting the two temperatures independently. This agreement supports the use of the model to resolve the internal conduction-radiation interaction.

Figure 2e further decomposes the incident solar irradiance under steady stagnation into optical loss ($q_{loss,opt}''$), convective ($q_{loss,conv}''$) and long-wave radiative losses ($q_{loss,rad}''$) from the exposed aerogel surface, and heat losses through the side ($q_{loss,side}''$) and bottom ($q_{loss,bot}''$) insulation boundaries. At steady state, these energy pathways satisfy

$$S = q_{loss,opt}'' + q_{loss,conv}'' + q_{loss,rad}'' + q_{loss,ide}'' + q_{loss,bot}'' \quad (13)$$

The resulting energy balance residual was 0.91%, confirming numerical closure of the steady stagnation solution. The relative contribution of each pathway further identifies the dominant energy losses under stagnation.

### 3.2 Temperature field mediated non-additivity of conduction and radiation

Conduction and thermal radiation within the aerogel are linked through the temperature field that drives both processes. This interaction is quantified using the absorber and upper aerogel surface temperatures, together with heat fluxes at the aerogel-absorber interface and upper aerogel boundary, for conduction only, radiation only, and fully coupled cases during an irradiance step from 1,000 to 600 W $m^{-2}$.

At 1,000 W $m^{-2}$, the radiation only case reaches an absorber temperature of 268 °C, while the conduction only case reaches 252 °C (Figure 3a). When conduction and radiation are solved simultaneously, the absorber temperature decreases to 220 °C, which is 32 °C lower than the conduction only result and 48 °C lower than the radiation only result. The opposite trend occurs at the upper aerogel surface (Figure 3b). The coupled case reaches 41 °C, compared with 37 °C for conduction only and 33 °C for radiation only. Coupling therefore lowers the temperature concentrated at the absorber while increasing the temperature reached by the aerogel, indicating stronger redistribution of thermal energy across the receiver.

The same ordering is maintained after the irradiance decreases to 600 W $m^{-2}$. The absorber temperatures approach 190, 162, and 148 °C for the radiation only, conduction only, and coupled cases, respectively. The corresponding upper aerogel surface temperatures are 29, 31, and 33 °C. The coupled case thus remains cooler at the absorber and warmer at the aerogel surface during both irradiance stages. These differences develop throughout the transient response and persist after the irradiance step, rather than appearing only after the receiver reaches steady state.

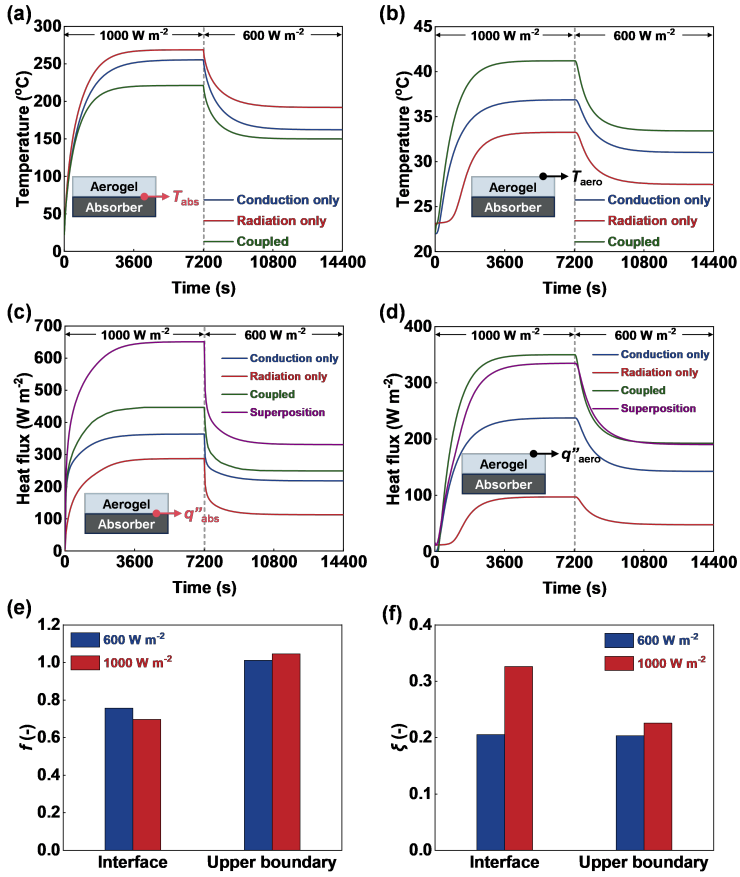


**Figure 3.** Transient conduction-radiation coupling during an irradiance step from 1,000 to 600 W m$^{-2}$. (a, b) Absorber and upper aerogel surface temperatures; (c, d) Heat fluxes at the absorber interface and upper boundary, including direct superposition; (e, f) Coupling factor and radiative fraction.

The effect of this temperature redistribution is more directly reflected by the heat flux at the aerogel-absorber interface. At 1,000 W m$^{-2}$, the conduction only and radiation only interface heat fluxes are 365 and 285 W m$^{-2}$, respectively (Figure 3c). Direct addition gives 650 W m$^{-2}$, whereas the fully coupled heat flux is only 445 W m$^{-2}$. The corresponding coupling factor is 0.69.

The coupled heat flux is therefore 31% lower than the directly superposed value. At 600 W m$^{-2}$, the conduction only and radiation only heat fluxes decrease to 215 and 110 W m$^{-2}$. Their sum is 325 W m$^{-2}$, compared with a coupled value of 250 W m$^{-2}$, giving $f_{abs}$ = 0.77 (Figure 3e). Direct superposition remains inaccurate at the lower irradiance, although the deviation decreases from 31% to 23%.

This non-additivity arises because the isolated heat fluxes are obtained from different temperature fields. At 1,000 W m$^{-2}$, the conductive flux is evaluated using the temperature field associated with an absorber temperature of 252 °C, whereas the isolated radiative flux is evaluated using a second field with an absorber temperature of 268 °C. Neither field exists when both transport modes are active. In the coupled case, radiative absorption redistributes energy within the aerogel and changes its temperature distribution. This modifies the gradient driving conduction. At the same time, the reduced absorber temperature lowers thermal emission and changes the radiative flux. The conductive and radiative contributions therefore adjust simultaneously until they are consistent with a shared temperature field. Adding the isolated fluxes instead combines transport rates associated with mutually incompatible thermal states.

The coupling behavior is markedly different at the upper aerogel boundary. At 1,000 W m$^{-2}$, the conduction only and radiation only heat fluxes are 235 and 95 W m$^{-2}$, giving a superposed value of 330 W m$^{-2}$ (Figure 3d). The fully coupled heat flux is slightly higher at 345 W m$^{-2}$, corresponding to $f_{aero}$ = 1.04. At 600 W m$^{-2}$, the superposed and coupled values are both close to 190 W m$^{-2}$, and $f_{aero}$ approaches unity.

The near-unity coupling factor at the upper boundary does not imply that conduction and radiation operate independently. At 1,000 W m$^{-2}$, the isolated and coupled cases still differ by up to 48 °C at the absorber and 8 °C at the aerogel surface. Instead, the near agreement in total heat flux results from compensating changes in conductive and radiative components as energy is transported through the aerogel. A superposition treatment can consequently appear accurate at the external surface while substantially overestimating heat transfer at the underlying absorber.

The radiative fraction further shows that coupling becomes stronger near the absorber as operating temperature increases (Figure 3f). At 600 W $m^{-2}$, radiation contributes 20% of the coupled heat flux at both evaluation locations. When irradiance increases to 1,000 W $m^{-2}$, the radiative fraction at the absorber interface rises to 0.33, whereas that at the upper aerogel boundary increases only to 0.23. Radiation therefore becomes increasingly important near the hotter absorber, while conduction remains the dominant transport mode at the external surface.

These results demonstrate that the accuracy of direct superposition depends on both the operating condition and the evaluation location. At the aerogel-absorber interface, superposition overestimates the coupled heat flux by 23-31% over the investigated irradiance range. At the upper boundary, the same treatment gives an apparently accurate total heat flux because internal coupling effects largely compensate before heat reaches the surface. This behavior is consistent with coupled conduction-radiation analyses showing that the two transport modes must be evaluated using their common temperature field rather than reconstructed from independently calculated thermal states[20].

### 3.3 Spatial temperature redistribution underlying the coupling effect

Figure 4 shows the steady temperature fields responsible for the location-dependent coupling identified in Figure 3. At 1,000 W $m^{-2}$, the maximum absorber temperature is 252 °C for conduction only and 268 °C for radiation only, but decreases to 220 °C when the two modes are coupled. The coupled temperature is therefore 32 °C below the conduction only result and 48 °C below the radiation only result.

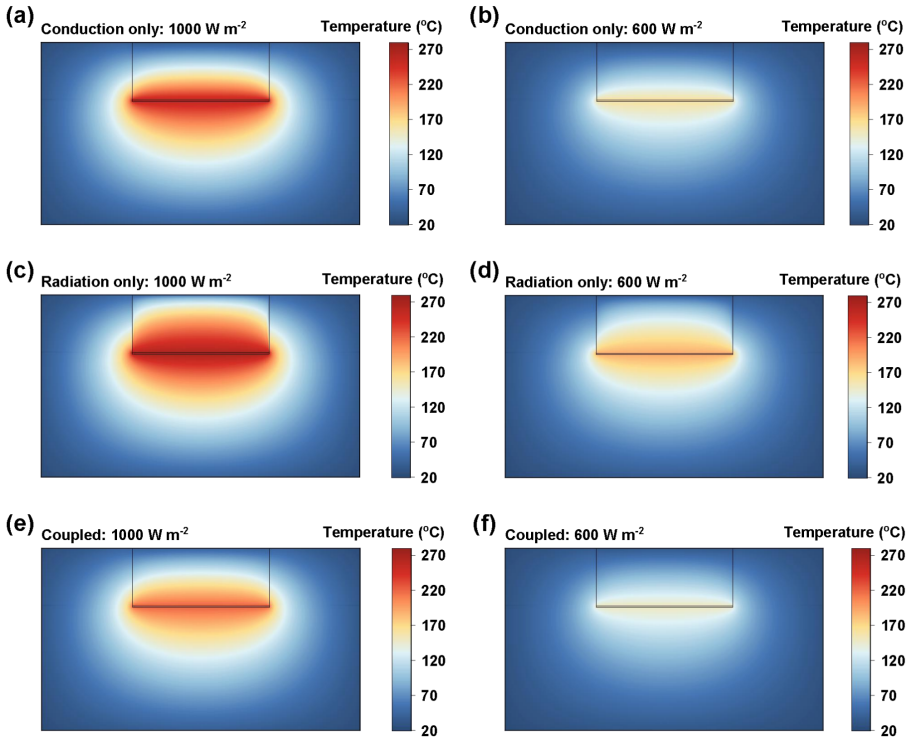


**Figure 4.** Steady temperature fields for (a, b) conduction only; (c, d) Radiation only; (e, f) fully coupled transport at 1,000 and 600 W $m^{-2}$. All panels use the same temperature scale.

The isolated modes also produce different spatial distributions. Conduction generates a smoothly decaying temperature field around the absorber, whereas radiation produces a more vertically extended heated region within the aerogel because thermal radiation is absorbed volumetrically. In the coupled case, this radiative energy deposition increases the aerogel temperature while reducing the temperature concentrated at the absorber. Accordingly, the upper aerogel surface temperature reaches 41 °C, compared with 37 °C for conduction only and 33 °C for radiation only. The resulting reduction in the absorber-to-aerogel temperature difference weakens the conductive gradient, while the lower absorber temperature simultaneously reduces radiative emission.

The coupling becomes weaker at 600 W $m^{-2}$. The absorber temperatures decrease to 162, 190, and 148 °C for the conduction only, radiation only, and coupled cases, respectively. The difference between coupled and conduction only temperatures therefore decreases from 32 °C at 1,000 W $m^{-2}$ to 14 °C at 600 W $m^{-2}$. Consistently, the radiative fraction at the absorber decreases from 0.33 to 0.20, while the coupling factor increases from 0.69 to 0.75. The lower operating temperature reduces both radiative transport and its feedback on the conductive temperature field.

The spatial redistribution also explains why the superposition error is much smaller at the upper aerogel boundary. At 1,000 W $m^{-2}$, the coupled and superposed surface heat fluxes are 345 and 330 W $m^{-2}$, giving $f_{aero}$ = 1.04. At 600 W $m^{-2}$, both values are close to 190 W $m^{-2}$. Although coupling strongly modifies the temperature field near the absorber, changes in conductive and radiative contributions largely compensate as heat propagates through the aerogel. The near unity surface coupling factor therefore results from spatial compensation rather than independent heat transfer modes.

### 3.4 Flow-rate dependence of thermal gain and response dynamics

Flow velocity changes both the fluid heat capacity rate and residence time within the receiver. It therefore controls not only the attainable outlet temperature rise but also the rate at which the outlet responds to a change in solar irradiance.

During the first 3,600 s at an irradiance of 1,000 W $m^{-2}$, increasing inlet velocity from 2 × $10^{-4}$ to 1.2 × $10^{-3}$ m $s^{-1}$ reduces the steady outlet temperature from 127 to 44 °C (Figure 5a,b,c,d,e,f). For an inlet temperature of 22 °C, the corresponding temperature rise decreases from about 105 to 22 °C. The absorber temperature decreases concurrently from 120 to 42 °C, whereas the upper aerogel surface temperature changes only from 32 to 24 °C. After irradiance is reduced at 3,600 s, the outlet temperature decreases from 86 to 36 °C over the same velocity range.

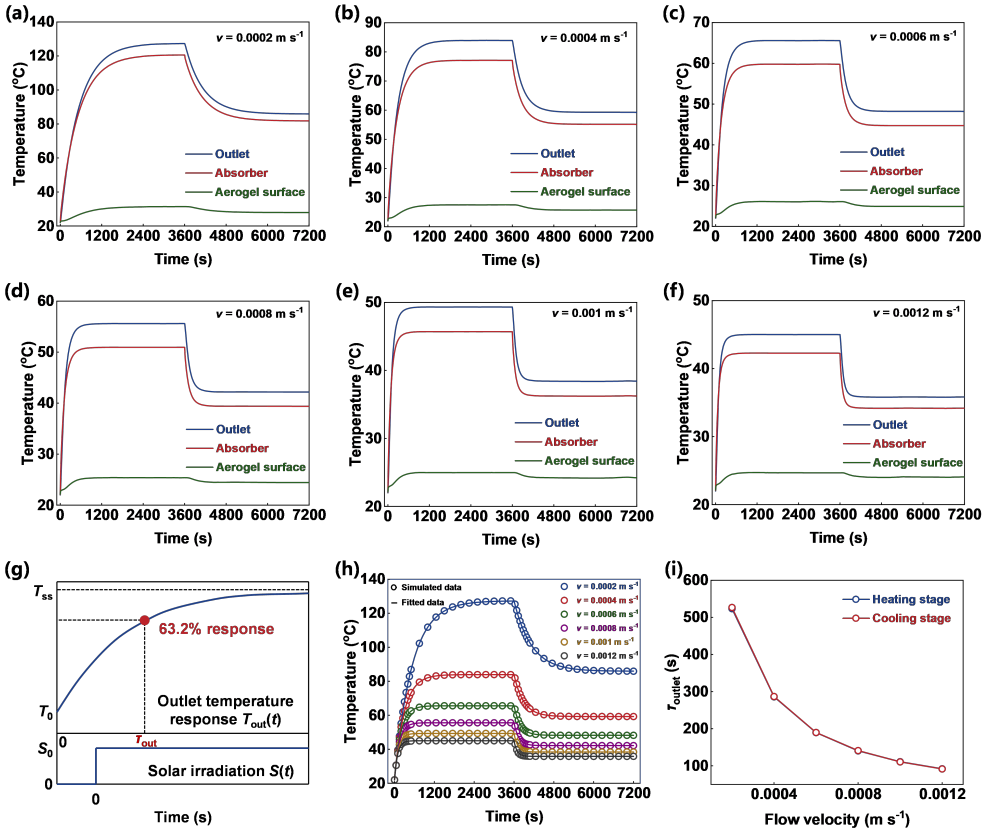


**Figure 5.** Flow-dependent fluid-heating performance and characteristic response time. (a-f) Outlet, absorber, and upper aerogel surface temperatures under an irradiance step for 6 inlet velocities; (g) Operational definition of the 63.2% response time; (h) Calculated and fitted outlet temperature histories; (i) Heating and cooling response times as functions of inlet velocity.

The strong reduction in outlet temperature rise results from the increasing fluid heat capacity rate. At low velocity, the absorbed thermal power is transferred to a smaller mass flow rate, and the longer residence time allows a larger temperature increase. Increasing velocity distributes the available heat over a larger mass flow rate and reduces the time available for fluid heating. This effect is nonlinear. Increasing velocity from 2 × $10^{-4}$ to 4 × $10^{-4}$ m $s^{-1}$ lowers the outlet temperature at 1,000 W $m^{-2}$ by 43 °C, whereas increasing it from 1.0 × $10^{-3}$ to 1.2 × $10^{-3}$ m $s^{-1}$ produces a decrease of only about 5 °C.

The transient response was quantified using the time required for the outlet temperature to reach 63.2% of the total change between two steady states (Figure 5g). The calculated outlet temperature curves are well represented by the fitted responses across the investigated velocity range (Figure 5h). As shown in Figure 5i, the characteristic response time decreases from 520 s at 2 × $10^{-4}$ m $s^{-1}$ to about 285, 188, 140, 110, and 90 s as the velocity increases successively to 4 × $10^{-4}$, 6 × $10^{-4}$, 8 × $10^{-4}$, 1.0 × $10^{-3}$, and 1.2 × $10^{-3}$ m $s^{-1}$. A sixfold increase in velocity therefore reduces the response time by 83%.

The reduction is most pronounced at low velocities. Doubling the velocity from $2 \times 10^{-4}$ to $4 \times 10^{-4}$ m s$^{-1}$ shortens the response time by 235 s, whereas increasing it from $1.0 \times 10^{-3}$ to $1.2 \times 10^{-3}$ m s$^{-1}$ yields a further reduction of only about 20 s. Heating and cooling response times remain similar throughout the investigated range, indicating that the dominant response scale is governed primarily by flow-dependent heat removal and receiver thermal inertia rather than by the direction of the irradiance change. The complete heating and cooling response metrics, including steady outlet temperatures, response times, and fitting coefficients, are summarized in Tables S4, S5.

Flow velocity consequently imposes a clear trade-off between thermal gain and response speed. Low velocities provide a large outlet temperature rise but require several minutes to establish a new thermal state. Higher velocities substantially accelerate the response, but the increased fluid heat capacity rate limits the delivered temperature rise. Both effects must therefore be considered when selecting the operating flow under variable solar input.

### 3.5 Dynamic flow regulation under measured *GHI* fluctuations

The flow-adjustment interval determines how frequently inlet velocity is updated in response to changes in solar input. An excessively short interval may introduce a new setpoint before the outlet temperature has responded to the previous adjustment, whereas an excessively long interval delays adaptation to sustained changes in irradiance. Adjustment intervals of 60-300 s were therefore evaluated because they spanned a substantial portion of the flow-dependent response time range of 90-520 s identified in Figure 5. The resulting inlet velocity schedules are provided in Figure S16.

The steady operating map in Figure 6a relates *GHI*, inlet velocity, and outlet temperature. Its construction, interpolation, and extraction of the 50 °C setpoint relation are described in Section S7.3. To maintain a target outlet temperature of 50 °C, the required velocity increases from $4 \times 10^{-4}$ m s$^{-1}$ at 400 W m$^{-2}$ to $9 \times 10^{-4}$ m s$^{-1}$ at 1,000 W m$^{-2}$. Below the flow-on threshold of 262.5 W m$^{-2}$, the target temperature cannot be maintained within the investigated flow range, and flow is suspended. The regulation strategy was evaluated using three *GHI* profiles measured in Shenzhen, representing a moderately fluctuating condition with a brief low-*GHI* interruption, a strongly intermittent condition with an extended near-threshold period, and a predominantly sunny condition with short cloud-induced fluctuations. The *GHI* measurement system, sampling procedure, and selected irradiance profiles are described in Section S7.1, with the compact weather station shown in Figure S14.

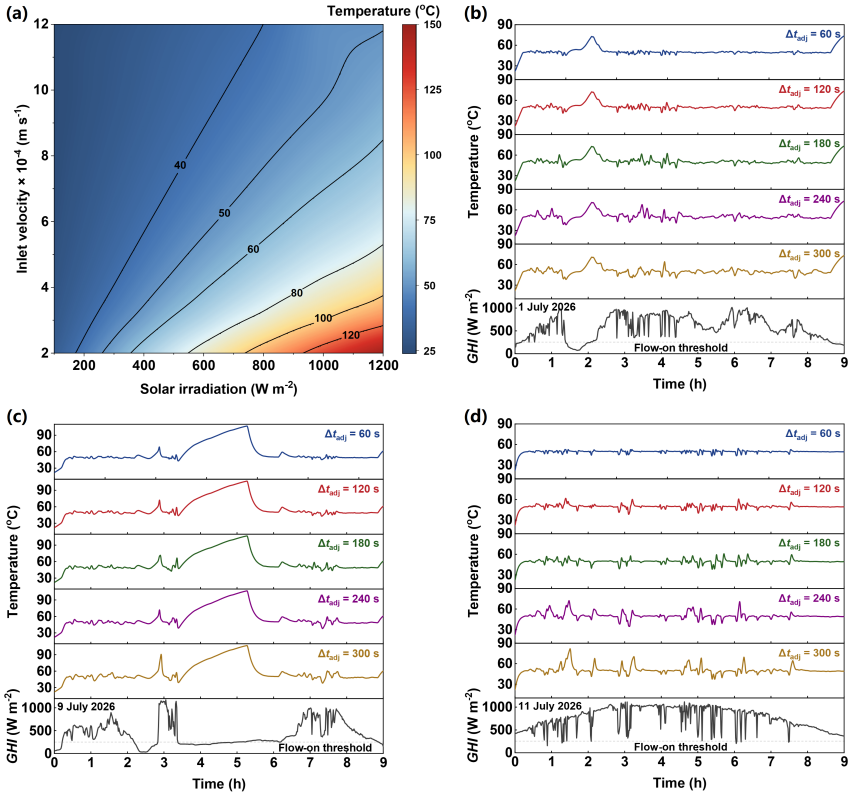


**Figure 6.** Dynamic flow regulation under measured Shenzhen *GHI*. (a) Steady operating map. Outlet temperature responses for 60-300 s update intervals under (b) moderate fluctuations, (c) strong near-threshold intermittency, and (d) predominantly sunny conditions. *GHI*: global horizontal irradiance.

For the moderately fluctuating profile, with a mean *GHI* of 577 W m$^{-2}$, the outlet temperature remains close to 50 °C during most of the flow-on period for all 5 adjustment intervals (Figure 6b). The largest excursion occurs after the pronounced *GHI* decrease near

1.5 h, when flow is interrupted and subsequently restarted. The outlet temperature rises to 70 °C before returning toward the target. Similar peak temperatures obtained for adjustment intervals from 60 to 300 s indicate that this excursion is governed mainly by the transition between flow-off and flow-on operation and by thermal energy stored in the receiver, rather than by the update interval alone.

The strongly intermittent profile produces a substantially larger temperature excursion because it combines the lowest mean *GHI*, 425 W $m^{-2}$, with a prolonged period close to or below the flow-on threshold (Figure 6c). During this period, repeated threshold crossings cause the controller to alternate between active-flow and 0-flow states. When flow is suspended, convective heat removal from the absorber is largely eliminated, while the remaining solar input continues to increase thermal energy stored in the receiver and stagnant fluid. The subsequent recovery of *GHI* therefore begins from an elevated thermal state, and the newly imposed flow cannot immediately remove the accumulated energy. The outlet region temperature consequently rises to 100–110 °C before returning toward 50 °C. Because no feasible flow-controlled operating point exists below the threshold, reducing the adjustment interval alone cannot prevent this overshoot.

A different response is observed for the predominantly sunny profile, which has the highest mean *GHI* of 760 W $m^{-2}$ and remains within the flow-on region for most of the evaluated period (Figure 6d). *GHI* contains frequent but relatively short reductions associated with passing clouds. With a 60 s adjustment interval, the outlet temperature remains mostly between 45 and 55 °C. Increasing the interval progressively enlarges deviations from the target. At 300 s, the outlet temperature varies between 35 and 80 °C during the most strongly fluctuating period. Because prolonged flow interruption is absent, differences among the responses arise mainly from the delay between a change in *GHI* and the corresponding update in flow velocity. Shorter intervals therefore improve temperature tracking under rapidly changing but continuously controllable conditions.

The integrated thermal efficiencies under the three measured *GHI* profiles are summarized in Table 1 and are much less sensitive to the adjustment interval than the instantaneous outlet temperature. For the moderately fluctuating profile, efficiency ranges from 77.2% to 77.5%, corresponding to an absolute variation of only 0.3%. The corresponding ranges are 69.0–69.4% for the strongly intermittent profile and 80.9–81.4% for the predominantly sunny profile, with variations of 0.4% and 0.5%, respectively. By comparison, the difference between the lowest and highest efficiencies across the three *GHI* profiles exceeds 12%. The strongly intermittent profile with the lowest mean *GHI* produces efficiencies near 69%, whereas the predominantly sunny profile produces efficiencies above 80%.

**Table 1.** Integrated thermal efficiency under measured Shenzhen *GHI* profiles.

| Date | Mean *GHI* (W $m^{-2}$) | $\eta_{60s}$ (%) | $\eta_{120s}$ (%) | $\eta_{180s}$ (%) | $\eta_{240s}$ (%) | $\eta_{300s}$ (%) |
|---|---|---|---|---|---|---|
| 1 July 2026 | 577 | 77.4 | 77.4 | 77.2 | 77.3 | ***77.5*** |
| 9 July 2026 | 425 | 69.2 | 69.2 | 69.0 | ***69.4*** | 69.1 |
| 11 July 2026 | 760 | ***81.4*** | 81.3 | 81.2 | 81.1 | 80.9 |

*GHI*: global horizontal irradiance.

These results distinguish the effect of the adjustment interval from that of the irradiance regime. The interval primarily determines short-term temperature stability when the receiver remains within the controllable flow range. During prolonged low-*GHI* periods, however, the flow-on threshold and stored thermal state dominate the response, and more frequent updating provides limited benefit. Mean *GHI* and the duration of flow interruption have a much stronger influence on daily thermal efficiency than the selected adjustment interval.

## 4. Conclusion

A transient non-gray model was developed and validated for a transparent silica aerogel covered solar fluid heater. Under stagnation at 1,000 W $m^{-2}$, the model reproduced an absorber temperature of 220 °C and an upper aerogel surface temperature of 42 °C. The results show that conduction and thermal radiation interact through their shared temperature field and cannot be reconstructed by adding independently calculated heat fluxes. At the aerogel-absorber interface, direct superposition overestimates coupled heat flux by 23–31%. The much smaller discrepancy at the external aerogel surface results from spatial compensation between conductive and radiative transport, rather than independence of the two mechanisms.

Flow velocity simultaneously determines the attainable outlet temperature rise and dynamic response. Increasing the inlet velocity from $2 \times 10^{-4}$ to $1.2 \times 10^{-3}$ m $s^{-1}$ reduces the characteristic outlet response time from 520 to 90 s, but lowers outlet temperature from 127 to 44 °C at 1,000 W $m^{-2}$. Under measured Shenzhen *GHI* profiles, varying the adjustment interval from 60 to 300 s changes integrated thermal efficiency by at most 0.5%, although it can substantially affect short-term temperature deviations. During prolonged low-*GHI* periods, flow interruption and thermal energy retained by the receiver dominate the subsequent outlet response, so more frequent updating alone cannot prevent temperature overshoot. These findings show that dynamic regulation should account for both the flow-dependent response time and the instantaneous thermal state of the receiver.

## Supplementary materials

The supplementary material for this article is available at: Supplementary materials.

## Declarations

### Acknowledgements

The authors declare that OpenAI ChatGPT 5.6 was used solely for language polishing during manuscript preparation. It was not used for study design, numerical simulations, data processing or analysis, interpretation of results, or formulation of conclusions. All scientific content was developed, reviewed, and approved by the authors.

### Authors contribution

Li S: Methodology, formal analysis, investigation, data curation, validation, writing-original draft.
Yang N, Li F, Liu S, Li C: Formal analysis, data curation, validation.
Deng S, Lin M: Methodology, supervision, funding acquisition, writing-review & editing.

### Conflicts of interest

There are no conflicts to declare.

### Ethical approval

Not applicable.

### Consent to participate

Not applicable.

### Consent for publication

Not applicable.

### Availability of data and materials

The data and materials could be obtained from the corresponding author upon request.

### Funding

This work was supported by the National Natural Science Foundation of China (No. 52376191), the National Key Research and Development Program of China (No. 2024YFF0505803), the Postgraduate Arts and Sciences Top-notch Innovation Award Program for 2024 of Tianjin University (No. C1-2024-002), the Shenzhen Science and Technology Innovation Commission (No. GJHZ20210705141808026), the Guangdong Basic and Applied Basic Research Foundation (No. 2023A1515011595), the Guangdong Major Project of Basic and Applied Basic Research (No. 2023B0303000002), and the High level of special funds (No. G03034K001).

### Copyright

© The Author(s) 2026.

## References

1. Weinstein LA, Loomis J, Bhatia B, Bierman DM, Wang EN, Chen G. Concentrating solar power. Chem Rev. 2015;115(23):12797-12838. [DOI]
2. Du S, He YL, Li MJ, Liu ZB. Transient response performances and control strategy of porous volumetric solar receivers with different heat transfer fluids. Sol Energy. 2024;283:112984. [DOI]
3. Zhao L, Bhatia B, Yang S, Strobach E, Weinstein LA, Cooper TA, et al. Harnessing heat beyond 200 °C from unconcentrated sunlight with nonevacuated transparent aerogels. ACS Nano. 2019;13(7):7508-7516. [DOI][PubMed]
4. Wang L, Zheng Y, Gao DC, Jin Y, Zhang Y, Sun Y. Bioinspired solar membrane distillation guttation leaf with enhanced salt resistance and uniform vapor flux. Desalination. 2026;638:120597. [DOI]
5. Wang L, Ma X, Zhao Y, Jin R, Zheng H. Performance study of a passive vertical multiple-effect diffusion solar still directly heated by parabolic concentrator. Renew Energy. 2022;182:855-866. [DOI]
6. Günay AA, Kim H, Nagarajan N, Lopez M, Kantharaj R, Alsaati A, et al. Optically transparent thermally insulating silica aerogels for solar thermal insulation. ACS Appl Mater Interfaces. 2018;10(15):12603-12611. [DOI][PubMed]

7. Berquist ZJ, Gayle AJ, Dasgupta NP, Lenert A. Transparent refractory aerogels for efficient spectral control in high-temperature solar power generation. Adv Funct Mater. 2022;32(12):2108774. [DOI]
8. Du M, Yang H, Huang J, Tang G, Zhang X, Niu D. Effects of moisture content on the radiative properties and energy-saving performance of silica aerogel windows. Langmuir. 2024;40(38):20273-20283. [DOI][PubMed]
9. Ueoka R, Negoro M, Kurahashi A, Miyamoto R, Kanamori K. Transparent silicone aerogels: Innovation and functionality toward commercialization. ACS Appl Mater Interfaces. 2025;17(32):45302-45322. [DOI][PubMed]
10. Li S, Liu S, Yang Q, Deng S, Lin M. Cover matters: Enhanced performance of a multistage solar evaporator with tuned optical and thermal cover properties. Energy Environ Sci. 2025;18(1):275-283. [DOI]
11. Abebe AM, Biesuz M, Vakifahmetoglu C, Cassetta M, Martucci A, Sorarù GD. SiOC ceramic aerogels with high optical transparency and ultralow thermal conductivity for solar power application. J Mater Chem A. 2025;13(39):33947-33957. [DOI]
12. Wang W, Li Q, Gao M, Wang K, Wu X, Bai Z, et al. Trimode integrated solar-thermal stacked converters for sustainable active buildings. ACS Sustainable Chem Eng. 2025;13(31):12458-12468. [DOI]
13. Li S, Zhang J, Chen Y, Liu S, Lu W, Deng S, et al. Tuning radiative properties of multiscale porous transparent silica aerogels for efficient solar interfacial evaporation. Adv Funct Mater. 2026;36(27):e28287. [DOI]
14. Li Q, Zhang Y, Wen ZX, Qiu Y. An evacuated receiver partially insulated by a solar transparent aerogel for parabolic trough collector. Energy Convers Manag. 2020;214:112911. [DOI]
15. Li X, Li R, Chang H, Zeng L, Xi Z, Li Y. Numerical simulation of a cavity receiver enhanced with transparent aerogel for parabolic dish solar power generation. Energy. 2022;246:123358. [DOI]
16. Qiu Y, Zhang Y, Li Q, Xu Y, Wen ZX. A novel parabolic trough receiver enhanced by integrating a transparent aerogel and wing-like mirrors. Appl Energy. 2020;279:115810. [DOI]
17. Zhao Y, Tang GH, Du M. Numerical study of radiative properties of nanoporous silica aerogel. Int J Therm Sci. 2015;89:110-120. [DOI]
18. Pajonk GM. Transparent silica aerogels. J Non Cryst Solids. 1998;225:307-314. [DOI]
19. Lee KH, Viskanta R. Transient conductive-radiative cooling of an optical quality glass disk. Int J Heat Mass Transf. 1998;41(14):2083-2096. [DOI]
20. Perraudin DYS, Haussener S. Numerical quantification of coupling effects for radiation-conduction heat transfer in participating macroporous media: Investigation of a model geometry. Int J Heat Mass Transf. 2017;112:387-400. [DOI]
21. Chow TT. Performance analysis of photovoltaic-thermal collector by explicit dynamic model. Sol Energy. 2003;75(2):143-152. [DOI]
22. Liu S, Yang B, Yu X. Thermal-hydraulic transient performance and dynamic characterization analysis of direct steam generation for parabolic trough solar collectors. Sol Energy Mater Sol Cells. 2025;279:113250. [DOI]
23. Hey JE, Hodson SL, Yazawa K, Doty J, Fisher TS. Experimental characterization of dynamic heat exchanger behavior. Int J Heat Mass Transf. 2018;121:933-942. [DOI]
24. Soto E, García J, Arévalo R, Barraza R, Soo Too YC. Performance analysis of a predictive control strategy for a simulated central tower CSP plant using real-time solar radiation measurements. Energy Convers Manag. 2026;348:120734. [DOI]

## Publisher's Note

Science Exploration remains a neutral stance on jurisdictional claims in published maps and institutional affiliations. The views expressed in this article are solely those of the author(s) and do not reflect the opinions of the Editors or the publisher.